Biophysical Journal Volume 93 November 2007 3034–3045

Atomic Resolution Modeling of the Ferredoxin:[FeFe] Hydrogenase Complex from *Chlamydomonas reinhardtii*

Christopher H. Chang, Paul W. King, Maria L. Ghirardi, and Kwiseon Kim
National Renewable Energy Laboratory, Golden, Colorado

ABSTRACT The [FeFe] hydrogenases HydA1 and HydA2 in the green alga *Chlamydomonas reinhardtii* catalyze the final reaction in a remarkable metabolic pathway allowing this photosynthetic organism to produce H_2 from water in the chloroplast. A [2Fe-2S] ferredoxin is a critical branch point in electron flow from Photosystem I toward a variety of metabolic fates, including proton reduction by hydrogenases. To better understand the binding determinants involved in ferredoxin:hydrogenase interactions, we have modeled *Chlamydomonas* PetF1 and HydA2 based on amino-acid sequence homology, and produced two promising electron-transfer model complexes by computational docking. To characterize these models, quantitative free energy calculations at atomic resolution were carried out, and detailed analysis of the interprotein interactions undertaken. The protein complex model we propose for ferredoxin:HydA2 interaction is energetically favored over the alternative candidate by 20 kcal/mol. This proposed model of the electron-transfer complex between PetF1 and HydA2 permits a more detailed view of the molecular events leading up to H_2 evolution, and suggests potential mutagenic strategies to modulate electron flow to HydA2.

INTRODUCTION

The current energy usage in the United States is heavily dependent (66%) on carbonaceous fossil fuel sources (coal, heating oil, natural gas), with minority contributions from nuclear, hydrological, or alternatives. All of these alternative technologies possess limitations to deployment, and it is widely accepted that the combustion by-products of carbonaceous fuels are accelerants of global climate change, with CO_2 giving rise to the majority of radiative forcing (1). Whereas production of ethanol and diesel fuels from renewable biomass is promising, there are questions about the timeframe for wide deployment as well as overall capacity and sustainability (2–5).

Thus, the problem of future energy supply is far from solved, and research on further technologies to address it are yet of keen interest. Among possible molecular energy carriers, dihydrogen (H_2) is a potentially pollution-free example. In addition to the challenges of storing adequate quantities on-site safely and efficiently (6), high-yield production from renewable feedstocks has not yet been achieved. To this end, a promising means of coupling terrestrial insolation to H_2 production is to exploit certain photosynthetic organisms' ability to catalyze H_2 evolution. Several species of green algae have been shown to possess this ability (7,8), including *Scenedesmus obliquus* (9), *Chlorella fusca* (10), and the free-living unicellular alga *Chlamydomonas reinhardtii* (11). Hydrogen production in the latter has been particularly well studied (12–18), and the requirements for maturation and heterologous expression of its two [FeFe] hydrogenases identified (19–21). The natural function of these enzymes in *Chlamydomonas* has been proposed to be an electron valve (22), allowing dissipation of excess reductant when CO_2 fixation is compromised.

Two [FeFe] hydrogenase isoenzymes, HydA1 and HydA2, are expressed in *C. reinhardtii* during periods of intracellular anaerobiosis, consistent with the O_2-lability of these enzymes (23,24). The incompatibility of [FeFe] hydrogenase activity and oxygenic photosynthesis is an obvious barrier to light-driven H_2 production. Ongoing efforts to circumvent it include temporal separation of light harvesting and H_2 evolution through reversible and partial inactivation of Photosystem II via sulfur nutrient deprivation (11,12,15,25), classical chemical mutagenesis, selection, and screening of *C. reinhardtii* mutants with more O_2-tolerant H_2 evolution (26), and molecular dynamics simulations to identify gas access channels within the hydrogenase structure as targets for mutagenic closure (27,28). It is envisioned that this research will lead to the development of a hydrogenase that is sufficiently tolerant to O_2 inactivation such that reduced degradation rates would enable sustained H_2 production in the presence of photosynthetically produced O_2. That being the case, the next potential gain in efficiency of H_2 photoproduction will depend on ensuring that most of the reductant generated by photosynthetic water oxidation will partition into the hydrogenase pathway and away from competitive reactions (17).

The primary electron donor for proton reduction by the *C. reinhardtii* [FeFe] hydrogenases is reduced [2Fe-2S] ferredoxin, which mediates electron transfer from the photosynthetic electron transport chain to reductive cellular metabolism (29). In the green algal chloroplast, ferredoxin plays a central role in the allocation of low-potential electrons from photosynthesis (30). This centrality can be viewed as a liability from the standpoint of maximizing photobiological H_2 production, as total electron flux is necessarily branched among

---

Submitted March 13, 2007, and accepted for publication July 6, 2007.

Address reprint requests to C. H. Chang, E-mail: christopher_chang@nrel.gov.

Editor: Ruth Nussinov.

0006-3495/07/11/3034/12 $2.00

doi: 10.1529/biophysj.107.108589

various competing assimilatory pathways. These pathways include CO_2 fixation, nitrite reduction, glutamate synthesis, sulfite reduction, cyclic electron transport around Photosystem I, and reduction of thioredoxin for regulation of biosynthetic pathways. The primary competitor with [FeFe] hydrogenase for low-potential electrons under physiological, aerobic conditions would be ferredoxin-NADP$^+$ oxidoreductase (FNR), the enzyme responsible for adapting one-electron metabolism to hydride-based anabolic metabolism such as CO_2 fixation.

Reduced *C. reinhardtii* FNR exhibits a Michaelis constant (K_M) for ferredoxin of 2.6 μM when coupled to cytochrome *c* reduction, with a dissociation constant obtained from fluorescence measurements of 25 μM (31). This reaction is the reverse of the physiological one in the chloroplast under carbon-fixing conditions, however. NADPH production by FNR from field horsetail shows a hyperbolic saturation with $K_M = 0.6$ μM (32). A large positive entropy change and small negative heat capacity change were associated with binding, suggesting an important role for desolvation in complex formation (33), with concomitant loss of catalytic cluster solvent accessibility (34). Binding was also weakened with increase in pH, reaching a new limiting strength at higher pH values which suggests protonation during complex formation (35). Increasing ionic strength was found to weaken the spinach ferredoxin:FNR complex, suggesting predominantly electrostatic interactions between ferredoxin and FNR. Based on chemical modifications, cross-linking, substrate binding, and NMR studies, it has been shown that the interaction between ferredoxin and FNR depends on negative charges in the former and positive charges in the latter (see (30) and references therein). Indeed, existing protein complex models propose a complementary fit between oppositely charged regions in the two proteins (36,37), and have been confirmed by various techniques (30). Recently, a crystal structure of the ferredoxin: FNR complex from maize was determined (38), demonstrating that the contact site close to the catalytic centers is hydrophobic, and that the orientation of the two proteins is determined by five intermolecular salt bridges.

Interestingly, the binding of ferredoxin to glutamate synthase ($K_M = 2$ μM) or nitrite reductase ($K_M = 20$ μM) (39) has been proposed to involve the same ferredoxin surface implicated in FNR binding, and to be similarly dependent on electrostatic interactions between negative charges on ferredoxin with positive charges on the other two proteins. Models for the docking of ferredoxin to the spinach nitrite reductase yielded solutions that confirm the proposed interactions (40). The binding of ferredoxin to sulfite reductase, an enzyme that has high structural homology to nitrite reductase (41), probably depends on a similar binding mechanism. Recent NMR and site-directed mutagenesis experiments revealed that there are differences in the specific ferredoxin amino-acid residues actually involved in the binding of each protein. The K_M for ferredoxin estimated by NADPH oxidation using a coupled FNR-ferredoxin-sulfite reductase assay was 4 μM (42). The binding of ferredoxin to ferredoxin:thioredoxin oxidoreductase (FTR), although still dependent on electrostatic interactions, seems to involve a smaller region on the surface of ferredoxin, and thus less dependence on ionic strength (43), but still yielding a low K_M of ~1.7 μM (39). The complementary binding surfaces on FTR are not known yet.

The interaction mechanism of green algal ferredoxins with [FeFe] hydrogenases has been less well characterized than the above examples. Homology modeling of the *Scenedesmus obliquus* [FeFe] hydrogenase and comparison to the *Scenedesmus vacuolatus* ferredoxin crystal structure led Florin et al. to postulate electrostatic complementarity as a dominant feature of ferredoxin-[FeFe] hydrogenase interactions (9). The K_M for *C. reinhardtii* [FeFe] hydrogenase-catalyzed H_2 production with reduced ferredoxin has been reported as 35 μM (purified HydA1 with spinach ferredoxin) (44) and 10 μM (partially purified HydA1/HydA2 mixture and *C. reinhardtii* ferredoxin) (45). Thus, to the extent that K_M reflects binding, the extant literature shows competitive ferredoxin binding affinity for its various partners, suggesting a potential target for optimization of biological H_2 production.

In support of future metabolic engineering efforts and detailed characterization of *C. reinhardtii* enzymes, this study is designed to characterize in detail the molecular interaction determinants between the *C. reinhardtii* [FeFe] hydrogenase isozyme HydA2 and [2Fe-2S] ferredoxin. To this end, we have constructed homology models of these two proteins, docked them together as rigid bodies, and calculated differential binding free energies between two competing models using an MM-(PB/GB)SA methodology. Interface characteristics and residue-level binding interactions of both models are analyzed, and a model most representative of the physically relevant ferredoxin-hydrogenase electron transfer complex proposed.

METHODS

Conceptually, our overall approach is a combination of the lock-and-key protein binding model for initial docking, followed by local induced fit as reflected in average structures over molecular dynamics trajectories (46). Visualization and structure manipulation was performed with the software packages Deepview (47) and visual molecular dynamics (48).

Homology modeling

Amino-acid residue numbering is relative to the N-terminal residue in the full-length DNA translation including the chloroplast signal transit peptide for both ferredoxin (GenPept records AAC49171.1 and PDB accession 1FCT) (49,50) and hydrogenase (GenPept record AAL23573) (16). The SWISS-MODEL worldwide web server (47,51,52) was used to construct the baseline homology models. The *C. reinhardtii* PETF1 [2Fe-2S] ferredoxin was modeled from Met-31 through Tyr-126, based on high sequence identity to the template models (spinach PDB code 1A70, *Anabaena* 7119 chain A, PDB code 1CZP, and *Anabaena* 7120 PDB code 1FRD). The HydA2 model was generated as described previously (13). The baseline homology models were refined through energy minimization and molecular dynamics as part of the SWISS-MODEL ProModII component (53), and the resulting structures used as input for docking calculations.

Docking

The program suite 3D-Dock (54–57) was used to generate 10,000 candidate protein complexes. The FT-DOCK component of this package implements the Katchalski-Katzir method for rapid matching of surface complementarity (57) with a grid-based electrostatic filter employing a distance-dependent dielectric (54). The metalloclusters of ferredoxin and HydA2 were not considered during the docking process. This initial set of structures was filtered to limit the maximum distance between HydA2 residue Cys-228 and ferredoxin residue Cys-69 (the [FeS] cluster ligands nearest to the surface of each protein) to <15 Å. This distance was sufficient to screen out the majority of poor candidates while avoiding erroneous rejection. The remaining 56 candidates were visually screened, leaving 16 possibilities. These were subjected to interfacial side-chain refinement with the MULTIDOCK component of 3D-Dock (56). The two complexes of lowest energy, labeled as complexes 16 and 42 based on their index numbers, were considered for further quantitative analysis. The complexes are related by an ~180° rotation about the ferredoxin [2Fe-2S]-HydA2 [4Fe-4S/H] intercluster axis.

Interface analysis

Visual and surface analyses were performed on the dynamics-averaged structures of complexes 16 and 42. Overall properties of the protein interfaces in complexes 16 and 42 were evaluated using the Protein-Protein Interaction Server (http://www.biochem.ucl.ac.uk/bsm/PP/server/) (58). For easier visualization, the Intersurf plug-in for VMD (59,60) was modified slightly to expand the color-encoding options. This analysis colors a surface with reference vertices defined as the midpoint between van der Waals surfaces of atoms connected by shortest possible line segments, generated by a Delaunay tetrahedralization of the interprotein volume (59). This surface is therefore approximately equidistant from both proteins. Each reference vertex was colored based on the interaction type between its associated atoms: aliphatic-aliphatic, aliphatic-charged, like charged, opposite charged, charged-polar, or aromatic-aromatic, with a distance cutoff of 8.0 Å applied.

Binding free energy calculations

Fig. 1 *A* illustrates the thermodynamic cycle used to calculate the solvated binding energies. We loosely followed the procedures outlined in Noskov and Lim (61). Pressure-volume work is taken from the ideal gas law as −0.6 kcal/mol based on $T = 303$ and $\Delta n = -1$ upon protein binding. Translational and rotational entropy changes are also calculated from gas-phase statistical mechanical relationships (61,62). Principal moments of inertia were calculated with VMD (63) and the Orient plug-in. The use of gas-phase equations is justified in that although rigid-body protein motions will be slower by virtue of interactions with solvent, the entropies are not dependent on the velocity of these motions. The standard solute concentration was taken as 10 μM, in contrast to the practice of taking the gas-phase standard-state value of 1 M—a simple volumetric calculation confirms the physical impossibility of 1 M ferredoxin (the smaller of the two proteins) at standard pressure.

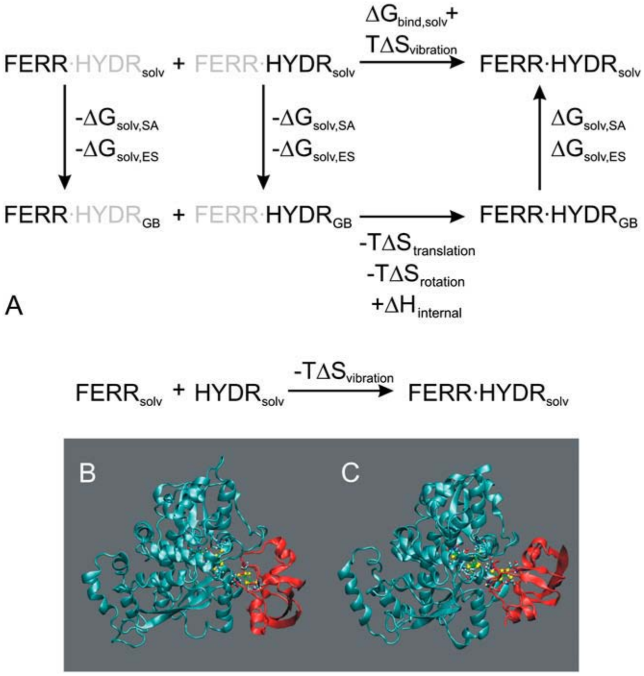

FIGURE 1 (*A*) The thermodynamic cycle considered, with the calculation methods for each step shown. Associated shaded text implies calculation of energy for the individual protein component (*solid text*) from the dynamics trajectory of the docked complex. Vibrational free energy changes were calculated from molecular dynamics runs on the free proteins. (*B*) Model complex 16. (*C*) Model complex 42.

Energy minimization and molecular dynamics in explicit water

Molecular dynamics and classical mechanical energy minimizations in explicit solvent were performed using the NAMD package (64). Protein models were constructed from PDB heavy-atom coordinates using VMD and the PSFGen plug-in. Proteins were solvated using the Solvate plug-in with a 12.5 Å pad of water, such that the minimum distance between protein image atoms under periodic boundary conditions was 25 Å. Sodium and chloride atoms were added to an ionic strength of 0.2 M using the Autoionize plug-in, which was sufficient to neutralize macromolecular net charge. Both δ-monoprotonated and (δ,ε)-diprotonated histidine residues were tested in the free energy calculations, but the latter gave unreasonably large binding energies. As all histidine residues in the individual proteins and complexes are well solvated at the protein surface and catalytic turnover is efficient above pH ~7 ≡ $pK_{a,2}$(His), all histidine residues were modeled as δ-monoprotonated. We have used a charge model for the metalloclusters reflecting semireduced HydA2 and reduced ferredoxin, namely $H^{I,I}[4Fe\text{-}4S]^{2+}[2Fe\text{-}2S]^{2+}$. This work therefore reflects the second electron transfer process before evolution of dihydrogen.

Langevin molecular dynamics (65,66) simulations were carried out using particle-mesh Ewald electrostatics treatment (67,68) and rectangular prismatic periodic boundary conditions. Mesh density was set to ~1 point per ångström. After 10,000 steps of conjugate gradient minimization (coordinates available as Supplementary Material), systems were equilibrated three times consecutively for 50 ps each in the isothermal-isobaric ensemble, allowing only uniform expansion or contraction of the simulation cell. During the first equilibration step, all protein atoms were fixed; during the second step, only backbone atoms were fixed; and finally, all atoms were allowed to evolve freely. During this phase, the Langevin collision parameter γ_{damp} was set to 20 ps^{-1}. Production dynamics were done in the NVT ensemble with $\gamma_{\mathrm{damp}} = 5\ ps^{-1}$, and with cell dimensions retained from the end of the equilibration phase. Multiple timestepping with the symplectic r-RESPA integrator (69,70) was employed, with nonbonded interactions calculated every time step (1.0 fs), full electrostatics every 2.0 fs, and nonbonded pair-lists updated every 10 fs. A 10/12/14 cutoff scheme was used, with a switching function turned on ~10 Å, full cutoff at 12 Å, and pair-lists evaluated over 14 Å. All bonds were maintained at their starting lengths using the RATTLE algorithm for protein atoms (71), and the noniterative SETTLE algorithm for water O-H bonds (72), and hydrogen atoms were not coupled to the Langevin temperature bath. Trajectories of total duration 3 ns were generated, with snapshots being saved every 100 fs for further analysis.

Internal energy and reference structure calculation

Thermodynamic cycle calculations often use a vacuum reference structure, in which structures are optimized in a fictional, in vacuo form with no charge neutralization. However, one could imagine large forces at unphysically charged surface residues leading to unrealistic structural rearrangements. We instead calculated total and generalized Born solvation energies (strain energies, electrostatic, van der Waals) with the generalized Born/molecular volume (73,74) method over the saved dynamics trajectories. Internal energy for each snapshot was calculated by subtracting solvation from total energy, then the resulting values averaged. The implementation in the CHARMM32 program package was employed, with the CHARMM22 force field (75) modified to include the appropriate cluster parameters. Atom-based electrostatics with 94/98/99 cutoff scheme and generalized Born parameters taken from Dominy and Brooks (76) were used. Nonbonded pair-lists were rebuilt at each snapshot. The average structure over the dynamics trajectory was taken for calculation of rigid-body and Poisson-Boltzmann solvation energies.

To eliminate possibly large and spurious structural changes arising from the use of homology models, ferredoxin, and HydA2 internal energies and average structures were calculated by extraction of the individual proteins' coordinates from the complex trajectories and recalculation of their GBMV energies, as opposed to separate dynamics trajectories on the individual proteins. Thus, the calculated changes in rigid-body entropies, internal enthalpies, and solvation free energies upon binding reflect the docking of two proteins in time-averaged, preorganized conformations. Of course, the estimation of configurational entropy changes upon binding requires independent analysis of vibrational motion in the free versus complexed proteins, and was done using separate dynamics trajectories for the individual proteins and their complexes (see below).

Solvation energy

The electrostatic and apolar components of the solvation energy for protein and complex reference structures, corresponding to the vertical arrows in Fig. 1 *A*, were calculated with the adaptive Poisson-Boltzmann solver (77,78). The full nonlinear PB equation was used, with ionic strength set to 0.1 M, an internal protein dielectric constant of 1.0, and solvent dielectric of 78.54. Solvent-accessible surface areas were calculated separately with the acc tool of adaptive Poisson-Boltzmann solver, using a 1.4 Å probe radius, and the solvation energy calculated from the equation

$$\Delta G_{\mathrm{solv}} = \Delta G_{\mathrm{electrostatic}} + \Delta G_{\mathrm{apolar}} = (\Delta H_{\mathrm{electrostatic},\varepsilon=80} - \Delta H_{\mathrm{electrostatic},\varepsilon=2}) + \gamma \times SASA$$

with the surface tension coefficient γ_{SA} set to 7.2 cal/mol per Å^2 (79).

Reduced-basis quasiharmonic analysis

Configurational entropy was calculated within the quasiharmonic approximation (80). The entropic component of the free energy arising from vibrations is defined as

$$TS_{\mathrm{vibr}} = \sum_{\mathrm{j}=1}^{3\mathrm{N}-6} \left[\frac{h\nu_{\mathrm{j}}}{e^{\frac{h\nu_{\mathrm{j}}}{k_{\mathrm{B}}T}} - 1} - k_{\mathrm{B}}T \ln\left(1 - e^{\frac{-h\nu_{\mathrm{j}}}{k_{\mathrm{B}}T}}\right) \right].$$

The lowest frequency vibrations therefore contribute the most to the configurational entropy. Because the change in bond vibrations and angle-bending force constants upon protein-protein association is expected to be small when compared with changes in librational motion (primarily expressible as a sum of dihedral motions) and the higher frequency regimes of the latter, a reduced basis of heavy-atom dihedral motions was used (81,82). The cumulative molecular dynamics trajectory for each protein or complex was analyzed every 200 ps, as dynamics data became available. Cumulative calculated $TS_{\mathrm{vibration}}$ was plotted against simulation time, and fit to the equation

$$TS_{\mathrm{vibration}} = A + B(1 - e^{-t/\tau 1}) + C(1 - e^{-t/\tau 2}).$$

By extrapolating to infinite time *t*, a limiting estimate for the configurational entropy becomes ($A + B + C$). This dependence was used to extrapolate to infinite simulation time.

Role of water at ferredoxin:HydA2 interface

To assess the potential role of specific water-mediated interactions to complex stability, the reference model complexes were treated with the program DOWSER (83), which identifies cavities into which insertion of one or more water molecules decreases enthalpy. Because atomic positions are critical for this analysis, we chose to use unaveraged docked complex structures instead of dynamically averaged ones. Whereas doing so may miss larger cavities produced upon dynamic motion, more insight into possible residue interactions of qualitative interest is likely.

RESULTS AND DISCUSSION

For notational brevity when referencing amino-acid residues on protein X of complex Y, we use the signature $\mathrm{Aaa}_{\mathrm{XY}}$, where *Aaa* is the standard three-letter amino acid identifier, $\mathrm{X} \in \{F,H\}$, where *F* denotes ferredoxin and *H* the [FeFe] hydrogenase HydA2, and an optional $\mathrm{Y} \in \{16,42\}$, denoting either complex 16 or 42. After screening candidate protein complexes by their residue pair-potential score, MULTIDOCK side-chain refinement, closest-approach electron transfer distance, and qualitative visual assessment, two complexes were deemed reasonable predictions for catalytically active electron transfer complexes. Designated by their index numbers as complexes 16 and 42, they are shown in Fig. 1, *B* and *C*. Our challenge in constructing a provisional model for metabolic electron flow in *C. reinhardtii* leading to H_2 production therefore became to distinguish which of these two possibilities represented the better choice, i.e., the more representative structure in an ensemble of possible protein complexes leading to electron transfer from reduced [2Fe-2S] ferredoxin to the semireduced HydA2. A variety of criteria were considered, including buried surface area, relative amounts of polar and apolar buried surface area, and minimum distance between atoms competent for participation in electron transfer between the two proteins. For the latter property, we took the minimum distance between sulfur atoms of cysteine metallocluster ligands, one on each protein. The relevant data are presented in Table 1. Both complexes have approximately the same buried surface area per protein, ~900 Å^2. This is a typical value for transient enzyme complexes (1900–2000 Å^2 combined) (84), and slightly larger than ~800 Å^2 interfacial area per protein of the [2Fe-2S] ferredoxin:FNR complex from maize leaf (38). The proposed interfaces are found to have slightly more apolar character than is typical (84), which likely reflects the dynamic averaging and the relative mobility of surface residues. The gap volume for complex 42 is 1800 Å^3 greater than for complex 16, which either

TABLE 1 Structural criteria for ferredoxin: hydrogenase complexes

Complex-component	16-FERR	16-HYDR	42-FERR	42-HYDR
Buried solvent-accessible surface area (Å^2)	921	939	893	922
% polar/apolar	42/58	30/70	38/62	31/69
Gap volume (Å^3)	4275		6083	
Hydrogen bonds	5		5	
Minimum S–S distance (Å)	8.2		5.5	

reflects slightly worse structural fit, or greater participation of interfacial water molecules, discussed below. All in all, the general properties of the protein-protein interfaces in these two complexes do not definitively distinguish the quality of one over the other.

Much work has gone into determining detailed residue-level interactions between ferredoxin and its various metabolic partners. Chemical modification and peptide mapping studies of [2Fe-2S] ferredoxin highlighted reactive carboxylate residues in three sequence regions (85). Fig. 2 shows a sequence alignment of commonly studied ferredoxins, with residues shown to be involved in protein-protein interactions highlighted. The three regions found by chemical modification are seen as conserved clusters of Asp and Glu in Fig. 2. *Anabaena* 7120 ferredoxin residues E95 and F66 were demonstrated to be important for interactions with FNR and the nitrite and nitrate reductases from this organism (86). Maize ferredoxin was shown by NMR and site mutation to interact with sulfite reductase through residues E29, E30, D34, E92, E93, and E94 (42), and both FNR and sulfite reductase through D65, D66, and E92 (87). The spinach enzyme was shown to require carboxylate residues for interaction with nitrite reductase, and detection of a ternary complex among ferredoxin, cytochrome *c*, and FNR suggests that there are at least two distinct binding modes for ferredoxin to its partners (88). Chemical modification experiments later identified D26, E29, E30, D34, D65, and D66 as protected upon complex formation (36). Twelve different residues were identified by NMR chemical shift perturbation as interfacial between *Synechocystis* ferredoxin and FNR (89). Perhaps most relevant to this study, complex formation between *C. reinhardtii* ferredoxin and either nitrite reductase or glutamate synthase was compromised by the mutation D91K, or the simultaneous triple change D56A/E59Q/E60Q (90).

As Fig. 2 illustrates, both ferredoxin:HydA2 model complexes involve the same interfacial residues of ferredoxin that were identified experimentally. This is not surprising, as the asymmetric disposition of the [2Fe-2S] cluster in the ferredoxin structure makes the general docking surface fairly clear. However, there are subtle differences between the two models. A particularly suggestive one involves aspartate residues 95 and 96, which are found within 5 Å of HydA2 in complex 16, but not in 42. The participation of these residues in maize and spinach ferredoxin interactions with FNR and sulfite reductase together with their strong sequence conservation hints that complex 16 may better reflect a more relevant functional conformation. In fact, D95/96$_{F42}$ are not interfacial, being completely solvent-exposed and no closer than 10 Å to any HydA2 residue, K350$_{H42}$ being the nearest in the dynamically averaged structure.

Visual analysis of local interactions between ferredoxin and HydA2 in complexes 16 and 42 are shown in Fig. 3. Although an overall distinction between the complexes is difficult to discern, one may see hot-spots such as complementary or clashing charge-charge interactions that are not only indicative of the model's validity, but also highlight engineering targets for enhanced protein-protein interaction. However, this analysis combines atomic (for surface characterization) and residue (for atom classification) bases, so the aliphatic portions of glutamate, lysine, and arginine, for example, are counted as charged. Thus, visually striking regions may not reflect an equally striking physical clash. Table 2 summarizes poor contacts (charge repulsions or aliphatic burial of charge) as well as favorable interactions (charge attractions, hydrogen bonding, and hydrophobic burial) seen upon detailed inspection of the

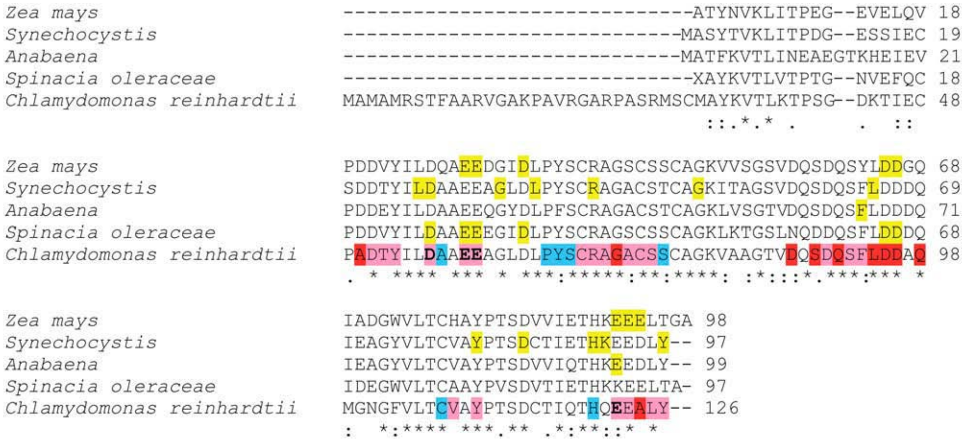

```
Zea mays                     ------------------------------ATYNVKLITPEG--EVELQV 18
Synechocystis                -----------------------------MASYTVKLITPDG--ESSIEC 19
Anabaena                     -----------------------------MATFKVTLINEAEGTKHEIEV 21
Spinacia oleraceae           ------------------------------XAYKVTLVTPTG--NVEFQC 18
Chlamydomonas reinhardtii    MAMAMRSTFAARVGAKPAVRGARPASRMSCMAYKVTLKTPSG--DKTIEC 48
                                                            ::.*.* .     .  ::

Zea mays                     PDDVYILDQAEEDGIDLPYSCRAGSCSSCAGKVVSGSVDQSDQSYLDDGQ 68
Synechocystis                SDDTYILDAAEEAGLDLPYSCRAGACSTCAGKITAGSVDQSDQSFLDDDQ 69
Anabaena                     PDDEYILDAAEEQGYDLPFSCRAGACSTCAGKLVSGTVDQSDQSFLDDDQ 71
Spinacia oleraceae           PDDVYILDAAEEEGIDLPYSCRAGSCSSCAGKLKTGSLNQDDQSFLDDDQ 68
Chlamydomonas reinhardtii    PADTYILDAAEEAGLDLPYSCRAGACSSCAGKVAAGTVDQSDQSFLDDAQ 98
                             . * **** *** * ***:*****:**:****: :*:::*.***:*** *

Zea mays                     IADGWVLTCHAYPTSDVVIETHKEEELTGA 98
Synechocystis                IEAGYVLTCVAYPTSDCTIETHKEEDLY-- 97
Anabaena                     IEAGYVLTCVAYPTSDVVIQTHKEEDLY-- 99
Spinacia oleraceae           IDEGWVLTCAAYPVSDVTIETHKKEELTA- 97
Chlamydomonas reinhardtii    MGNGFVLTCVAYPTSDCTIQTHQEEALY-- 126
                             :  *:**** ***.** .*:**::* *
```

FIGURE 2 Sequence alignment of selected [2Fe-2S] ferredoxins. Numbering of residues identified in the literature has been adjusted to match the sequences shown. Residues are highlighted to denote those experimentally identified as located at active electron transfer interfaces (*yellow*), and at the complex 16 (*red*), 42 (*light blue*), or 16 and 42 (*light purple*) interfaces in this study. *C. reinhardtii* residues in bold denote those interacting with nitrite reductase and glutamate synthase (90). Absolute and partial identities and functional conservation are denoted underneath the sequence blocks with symbols {*, .,:}, respectively.

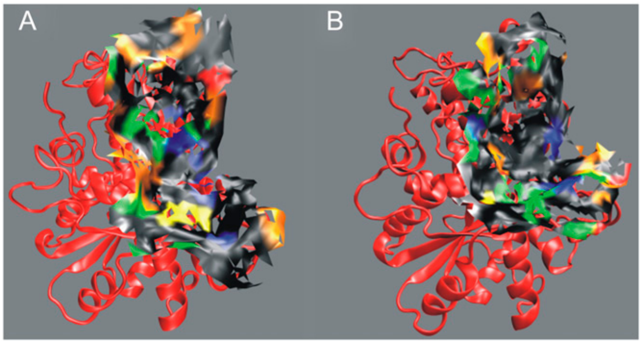

FIGURE 3 Interaction surfaces of complexes 16 (*A*) and 42 (*B*), color-coded by residue interactions. Hydrogenase HydA2 is oriented similarly in the two images for comparison, and the ferredoxin has been omitted for clarity. (Colors are: *red*, like charges; *orange*, charge-polar; *yellow*, aromatic-aromatic; *green*, charge-aliphatic; *blue*, aliphatic-aliphatic; *gray*, opposite charges.)

complexes in Fig. 3. Visual analysis shows complex 42 has more buried charge interactions than complex 16, indicating possible problems with the model. Most locally poor contacts are mitigated by one or more of several mechanisms, including salt-bridging, hydrogen-bonding, or surface disposition, which would allow bulk ionic screening. When these interactions are taken into account, complex 42 still has an unfavorable charge repulsion at the N-terminus; however, the placement of this portion of the protein by homology modeling and the relative dynamics freedom of polypeptide termini does not lend much weight to this single observation.

Complex 16 exhibits a greater number of favorable charge attractions, possibly suggesting a more natural complementarities of surfaces than the alternative model. Table 2 includes key observed side-chain interactions amenable to site-directed mutagenic testing for both models. Aside from targets disrupting salt bridges or hydrogen-bonding, both complexes show a single nonelectrostatic interaction feature that could permit less disruptive testing than changing charge or hydrogen bonding at the protein-protein interface. Complex 16 contains a hydrophobic pocket on the hydrogenase surface that envelops Phe-93 of ferredoxin; stepwise elongation of Ala-3 on hydrogenase would be expected to progressively disrupt binding affinity as well as electron transfer. On the other hand, complex 42 has hydrogenase Leu-403 tightly packed against Cys-74$_\text{F}$. Mutations that either truncate or elongate the former residue would be expected to disrupt electron transfer more so than binding affinity. Mutagenic testing of these latter two interactions should show substantial effects with subtle changes in aliphatic chain length, thereby simplifying interpretation. Furthermore, a significant interaction involving A65$_\text{H16}$ or L403$_\text{H42}$ with ferredoxin exists only in the corresponding model complex. Changing either residue by mutation would affect binding and/or electron transfer parameters only if the corresponding model is relevant.

TABLE 2 Contacts identified by Intersurf analysis

Complex	Residue(s)	Interaction type	Mitigating factors or comments
16	R70$_\text{F}$ – K408$_\text{H}$	Charge repulsion	Nearby D56$_\text{F}$/E59$_\text{F}$, surface
	D90$_\text{F}$	Uncompensated charge	Internal H-bonds to Y53, S89, Y110
	Y53$_\text{F}$ – M179$_\text{H}$	Potential H-bond	
	E59$_\text{F}$ – K408$_\text{H}$	Charge attraction	
	E60$_\text{F}$ – K412$_\text{H}$	Charge attraction	
	D87$_\text{F}$ – K182$_\text{H}$	Charge attraction	
	S89$_\text{F}$ – K182$_\text{H}$	Potential H-bond	
	D90$_\text{F}$ – R230$_\text{H}$	Charge attraction	
	F93$_\text{F}$	Hydrophobic pocket	Ala-3H → larger would disrupt
	D95$_\text{F}$ – K73$_\text{H}$	Charge attraction	
	Y110$_\text{F}$ – K407$_\text{H}$	Potential H-bond	
42	D51$_\text{F}$–D67$_\text{H}$	Charge repulsion	Surface, charge centers > 8 Å
	D56$_\text{F}$	Uncompensated charge	Salt bridges to R70$_\text{F}$, H71$_\text{H}$
	R70$_\text{F}$–K73$_\text{H}$	Charge repulsion	Surface
	A63$_\text{H}$	Uncompensated charge	
	D90$_\text{F}$–D443$_\text{H}$	Charge repulsion	Surface
	R230$_\text{H}$	Uncompensated charge	Surface
	K407$_\text{H}$	Uncompensated charge	H-bond to E122$_\text{F}$,L125$_\text{F}$ carbonyls
	D56$_\text{F}$ – H71$_\text{H}$	H-bond	
	E59$_\text{F}$ – K73$_\text{H}$	Charge attraction	
	Y67$_\text{F}$ – R168$_\text{H}$	Potential H-bond	
	C74$_\text{F}$ – L403$_\text{H}$	Tightly packed	Change would primarily affect ET
	D90$_\text{F}$ – K444$_\text{H}$	Charge attraction	
	Y110$_\text{F}$ – D67$_\text{H}$	H-bond	
	E122$_\text{F}$ – K182$_\text{H}$	Charge attraction	
	E122$_\text{F}$ – S183$_\text{H}$	Potential H-bond	
	Y126$_\text{F}$ – K412$_\text{H}$	Potential H-bond	

An obvious metric for the accuracy of a putative complex of electron transfer proteins is the distance between the closest atoms of each ET cofactor. It has been observed that direct ET through proteins, i.e., not involving intermediate radical species on amino-acid residues or oxidation/reduction of cofactors, generally has a maximum effective distance of 20 Å (91). The electron-carrying centers in both complexes are well within this maximum distance. Furthermore, the rate of electron transfer through an homogeneous medium is distance-dependent, such that candidate complexes with the smallest intercluster distances would be expected to transfer electrons fastest (92). The dynamic profile of the Cys66$_\text{F}$–C428$_\text{H}$ distance for both complexes is profiled in Fig. 4. In both cases, at least two conformations are observed, each with a different S–S distance. Ignoring the actual inhomogeneity of the protein medium, complex 42 would be expected to be the superior choice for in vivo H_2 production,

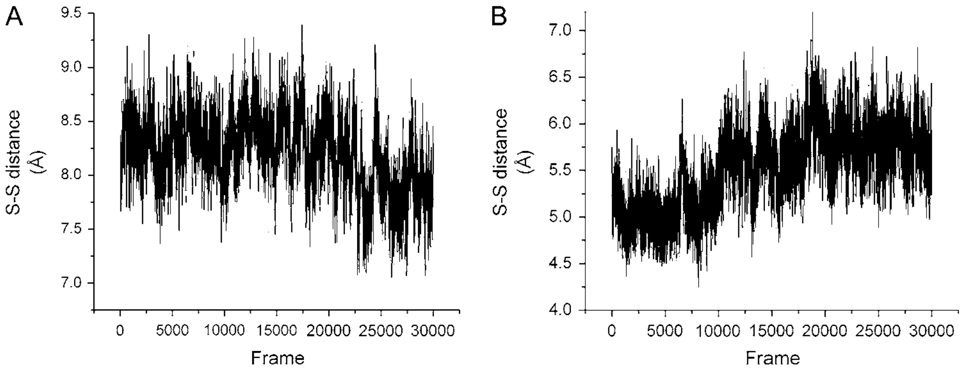

FIGURE 4 Timecourse of closest S–S approach distance between electron transfer cofactors on ferredoxin and hydrogenase HydA2 during molecular dynamics simulations for (*A*) complex 16, and (*B*) complex 42.

with dominant average S–S distances ranging between 5.0 Å and 6.0 Å. Complex 16 begins the dynamics trajectory at a high value near 8.5 Å, which decreases at ~2 ns to ~7.8 Å. However, this measure implicitly presumes that

1. Electron transfer is the overall rate-limiting reaction step for H_2 production; and
2. Evolution has selected biological function based on maximum catalytic rate.

Of course, if Assumption 1 is false, then distance as a metric is less convincing and Assumption 2 will favor complexes with another property besides maximal ET efficiency; if Assumption 2 is false, then another metric for selecting optimal complexes must be found as well. Our required use of homology models prevents us from assigning much weight to the difference in S–S distances as a determinant between the two competing models, and the potentially differentiating roles of dynamics and atomic arrangements between the two complex models await experimental structural determination. Nevertheless, taken at face value complex 42 would be expected to exhibit the faster ET rate once the protein complex is formed.

Dowsed models

The presence of large gap volumes and abundance of charged residues at the putative ferredoxin:HydA2 interface suggests that water molecules may play a role in bridging the two proteins in a productive ET complex. To examine this possibility, the candidate docked complexes were processed with the Dowser software, which iteratively finds cavities into which water may be inserted, then calculates a water orientation leading to a net decrease in enthalpy relative to the isolated species. Asp-90_{F16}, which is buried in the reference structure, is engaged in two hydrogen bonds to interfacial waters in the dowsed structure. This is the most solvent-inaccessible of the negative interactions present in complex 16, and this hydrogen-bonding would significantly reduce the negative impact of charge burial during complex formation. Nevertheless, the worrisome charge repulsion between Arg-70_{F16} and Lys-408_{H16} is not affected by additional water interactions. $N_{\eta 2}$ of Arg-230_{H42} is hydrogen-bonded through a water dimer to Ser-76_{F42}. The presence of these waters mitigates what appears to be an uncompensated charge in the un-Dowsed model complex. The same is true for Asp-56_{F42}, Arg-70_{F42}, and the N-terminal Ala-63_{H42}, which like Arg-230 is hydrogen-bonded to a water dimer.

Thus, it appears that the only unmitigated poor contact in complex 42, namely the uncompensated charge of Arg-230_H, may be relieved somewhat through hydrogen-bonding interactions. On the other hand, complex 16 has an uncompensated charge repulsion between Arg-70_F and Lys-408_H that is not likely in the test conformation to be relieved by aqueous interfacial interactions. With respect to distinguishing the two model complexes, then, an examination of water interactions favors complex 42 over 16.

Binding free energy

To evaluate further the relative quality of our two candidate models, we have calculated their approximate binding energy based on the MM-PBSA approach. Reference structures for all energy calculations except vibrational entropy changes were derived from structures in explicit solvent, averaged over 3 ns of all-atom dynamics. Binding free energies are summarized in Table 3. The translation entropy change for both complexes is necessarily identical, as this depends only on the protein and complex masses, which are conserved between

TABLE 3 Binding free energy results

Complex	16	42
$T\Delta S_{\mathrm{translation}}$*	−21.1	
$T\Delta S_{\mathrm{rotation}}$	−15.7	−15.7
$T\Delta S_{\mathrm{vibration}}$	−102.7	−78.4
$\Delta H_{\mathrm{internal}}$	−175.3	−68.3
$\Delta\Delta G_{\mathrm{solvation,electrostatic}}$	378.6	330.8
$\Delta\Delta G_{\mathrm{solvation,surface}}$	−15.8	−15.3
$\Delta G_{\mathrm{binding}}$	342.2	361.7

*$T\Delta S_{\mathrm{translation}}$ is the analytically the same for both complexes, as the complex and component masses are identical; $T\Delta S_{\mathrm{rotation}}$ is only coincidentally the same.

the two candidates. Loss of entropy requires this term to contribute unfavorably to the binding process, reflected in $T\Delta S_{\mathrm{translation}}$ being negative. The rotational entropy change is related to the change in moments of inertia between the individual proteins and the complex, and so could be different between the two complexes. However, both complexes are of similar overall shape, and $\Delta S_{\mathrm{rotation}}$ values were essentially the same. The only quantities in the expression for TS_{rotation} specific to molecular structure are the product of inertial moments; thus, the protein:protein complex will have a larger TS_{rotation} than the individual proteins due to possibly greater asymmetry in $I_{\mathrm{x,y,z}}$ implying more dissimilar configurations with respect to an external reference frame, and a larger system implying more distinct surface configurations per unit of solid angle. However, due to the loss of relative rotational freedom between the two proteins, rotational entropy results in a positive free energy contribution to binding.

Configurational entropies of the individual proteins and complexes were evaluated within a reduced basis quasiharmonic approximation, which was performed on trajectories generated from explicit solvent dynamics simulations. Thus, side-chain motions at the complex interfaces at least partially reflect the presence of exchangeable, buried water. Through short times, a single exponential dependence of $TS_{\mathrm{vibration}}$ was seen as the number of snapshots analyzed approached the expected number of dihedral modes. As more complete data became available and was included in the fitting, a double exponential dependence was discovered, with an apparent damped oscillation in the calculated energy apparent in the residuals (Fig. 5). Assuming this functional dependence holds approximately past the actual simulation endpoint allowed us to estimate the limiting $TS_{\mathrm{vibration}}$ at infinite simulation time. Formation of both complexes leads to a net loss of configurational entropy (Table 3), as might be expected by the additional motional constraints imposed on a protein surface by interaction with its binding partner. In fact, complex 16 formation results in a loss of 24.3 kcal/mol more vibrational free energy than complex 42, qualitatively consistent with slightly less buried surface area in complex 42 as compared to 16 in the dynamically averaged complex structures (Table 1).

The model complexes differed greatly in the values of their internal enthalpy, in which we include strain energy from internal coordinates, van der Waals repulsions, and internal electrostatic energy evaluated with large-distance cutoffs and a dielectric constant of 1 (i.e., an in vacuo evaluation at the reference geometry). Complex 16 shows a larger negative binding enthalpy than complex 42, despite the charge repulsion mentioned previously. This difference could be related directly to the interactions at the protein interfaces, or to internal rearrangements of the proteins resulting from the different external potentials connected with the divergent docking geometries. The former explanation is favored, based on consideration of solvation energies.

The surface area contributions to solvation energies slightly favor complex 16, by 0.5 kcal/mol. This number reflects the entropy associated with water release from the interface, and necessarily contributes a negative free energy change to binding. The differences in electrostatic solvation enthalpy between complexes 16 and 42 are more significant, with complex 16 favored by 47.8 kcal/mol over 42. The magnitudes of the values in Table 3 suggest that the complexes gain much less from solvation than the individual proteins, which might be expected from formation of ion pairs at the protein-protein interface. In our results, this energy is not compensated by binding enthalpy or entropic considerations.

The absolute binding free energies for the two complexes are unphysically large and positive, which is perhaps not

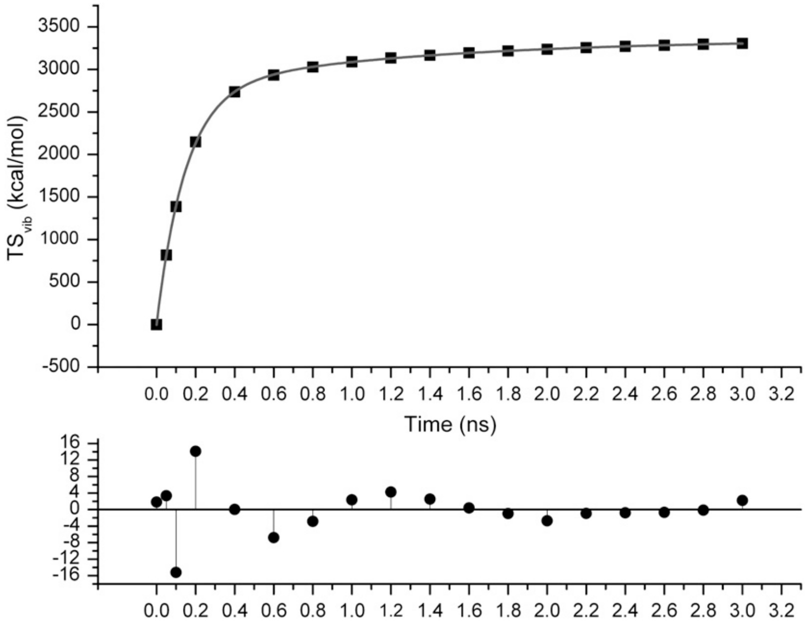

FIGURE 5 Plot of representative reduced-basis quasiharmonic analysis (*top*), and residuals (*solid circles*, *bottom*). Data (*solid squares*) were fit to a biexponential equation (*line*), and configurational entropy calculated by extrapolation of this equation to infinite time.

surprising considering the required use of homology modeling to derive these structures. Nevertheless, the calculated $\Delta\Delta G_{16\text{-}42} = -19.5$ kcal/mol is not outside the bounds of realism, and suggests that complex 16 is a better representation of the dominant binding conformation than complex 42. This is especially interesting in light of the closest approach distance between electron transfer centers, identified as the nearest cysteinyl S–S distance. For the averaged complex structures, this is listed in Table 1; the timecourses for this value in the two complexes are shown in Fig. 4. Complex 42 consistently has a shorter S–S distance than 16, which would imply a faster ET rate in the absence of specific medium effects or gating mechanisms. An obvious question is whether binding or inter-co-factor distances would have a greater effect on overall electron transfer. If we postulate a mechanism of the form

$$FERR_{\mathrm{red}} + HYDR_{\mathrm{ox}} \overset{\mathrm{K_{eq}}}{\rightleftarrows} FERR_{\mathrm{red}} \cdot HYDR_{\mathrm{ox}} \xrightarrow{\mathrm{k_{et}}} FERR_{\mathrm{ox}} + HYDR_{\mathrm{red}},$$

then the overall rate will be proportional to $K_{\mathrm{eq}}k_{\mathrm{et}}$. A difference in binding energy of -19.5 kcal/mol implies a ΔK_{eq} of

$$e^{-\frac{\Delta\Delta G_{16-42}}{\mathrm{RT}}} = e^{\frac{19.5}{1.987\times10^{-3}\cdot 303}} = 1.16\times10^{14},$$

favoring complex 16. Additionally, if electron transfer is taken to depend exponentially on distance (93) and a typical value of the constant β for biological electron transfers = 1.1 Å^{-1} is assumed (91), Δk_{et} between model complexes 16 and 42 may be calculated to be

$$\Delta k_{\mathrm{et}} = e^{-\beta\Delta \mathrm{r}} = e^{-2.97} = 5.13\times10^{-2}$$

using the S–S distances from Table 1. Clearly, assuming weak electronic coupling between ferredoxin and hydrogenase redox cofactors, the calculated binding energy advantage for complex 16 will trump the closer electron hopping distance in complex 42.

Finally, examination of the electrostatic isopotential surfaces for the free ferredoxin and HydA2, shown in Fig. 6, brings to light a not-unexpected charge complementarity between these two proteins. Both are seen to be predominantly negatively charged; however, a region of positive electrostatic potential (ESP) around the HydA2 catalytic clusters is evident. In addition, ferredoxin displays a substantial lobe of negative ESP projecting out from the [2Fe-2S] center. This suggests localized regions of opposite ESP help to 1), promote complexation between HydA2 and ferredoxin; and 2), discourage complex formation in geometries that are unproductive for electron transfer. Both of the candidate models have interaction surfaces mating the electronegative surface of ferredoxin with the electropositive surface on HydA2, suggesting that the docking models are globally correct.

CONCLUSIONS

Combined homology modeling, empirical protein docking, visual analysis, and quantitative binding free energy calculations have been used to distinguish between two competing protein-protein interaction models and to develop a working model for the likely interaction geometry between the [2Fe-2S] ferredoxin and [FeFe] hydrogenase 2 in the green alga *Chlamydomonas reinhardtii*. The exquisite balance of energies leading to protein complexation is difficult to evaluate simply through quick visualization, and thus more quantitative techniques can discriminate among and lend insight to even approximate structural models. Furthermore, a simple distance-based criterion for identifying a better electron transfer complex was demonstrated to fail in this case, within the limits of our model accuracy. Detailed analysis of the protein:protein interfaces leads us to put forward complex 16 as the best reference structure to consider more detailed interactions, such as the electron transfer mechanism and mutagenic engineering for enhanced protein function in vivo.

In this work, we have explored binding and dynamics directly relevant to the second of the two ET reactions between reduced ferredoxin and HydA2 necessary to complete one cycle of dihydrogen evolution catalysis. At present, no experimental

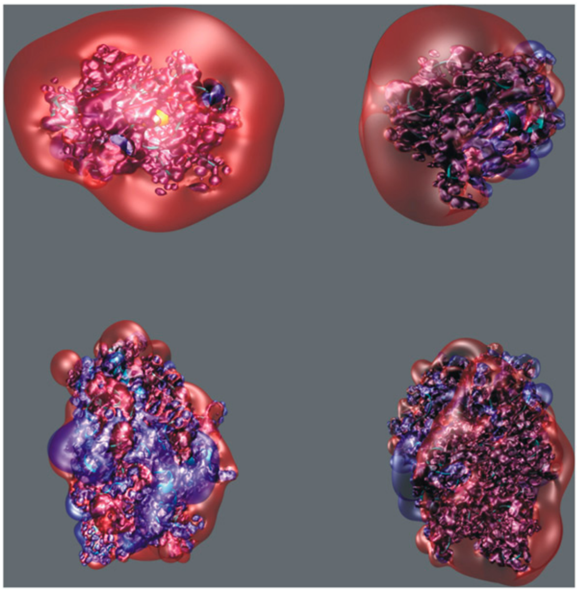

FIGURE 6 Electrostatic isopotential surfaces for ferredoxin (*top*) and HydA2 (*bottom*), contoured at $+1.0\ k_{\mathrm{B}}T/q_{\mathrm{e}}$ (*blue*) and $-1.0\ k_{\mathrm{B}}T/q_{\mathrm{e}}$ (*red*). Pictures on the left represent direct views of the protein-protein interface; those on the right are rotated by 90° clockwise about the vertical axis running through the protein and in the plane of the figure.

data is available to evaluate directly the importance of charge and protonation states on preferred conformations for these two proteins from *C. reinhardtii*. Also, certain details of cofactor structure such as the bridging ligand of the H-cluster (94–96) and putative hydride-binding conformation (97,98) are still uncertain. The role of these considerations on ferredoxin:HydA2 binding and electron transfer as well as the full biological context of ferredoxin-mediated H_2 production is the subject of ongoing investigation.

Despite these caveats, we view our model and data as a valuable starting point and guide for future investigations and molecular engineering studies to optimize the allocation of photosynthetic reductants to the H_2-production pathway in *C. reinhardtii*. It is clear, however, that the relative difficulty in acquiring experimental binding data on ET systems, and the potential convolution of electron transfer with binding, bring further complexity to this overall goal. We expect computational modeling of this system to couple tightly with experimental data to tease apart this complexity and yield a unified understanding of protein-protein interaction and ET function in the *Chlamydomonas* H_2-production pathway.

SUPPLEMENTARY MATERIAL

To view all of the supplemental files associated with this article, visit www.biophysj.org. Atomic coordinates of energy-minimized, desolvated ferredoxin:hydrogenase complex models 16 and 42 are available as PDB-format files. Dynamically averaged structure coordinates are available on request.

We thank Jordi Cohen and Professor Klaus Schulten for supplying metallo-cluster parameters.

This work was supported by the National Renewable Energy Laboratory Discretionary Research & Development program, and by the U.S. Department of Energy under contract No. DE-AC36-99GO10337 with the National Renewable Energy Laboratory. The United States Government retains, and the publisher, by accepting the article for publication, acknowledges that the United States Government retains a nonexclusive, paid-up, irrevocable, worldwide license to publish or reproduce the published form of this work, or allow others to do so, for United States Government purposes.

REFERENCES

1. Boucher, O., J. Haigh, D. Hauglustaine, J. Haywood, G. Myhre, T. Nakajima, G. Y. Shi, and S. Solomon. 2001. Climate change 2001: the scientific basis. *In* Radiative Forcing of Climate Change. V. Ramaswamy, editor. Intergovernmental Panel on Climate Change.
2. Dalgaard, T., U. Jørgensen, J. E. Olesen, E. S. Jensen, E. S. Kristensen, D. Connor, I. Mínguez, T. H. Deluca, and S. E. Koonin. 2006. Looking at biofuels and bioenergy. *Science*. 312:1743–1744.
3. Brower, K. R., B. H. Davison, A. J. Ragauskas, R. Templer, T. J. Tschaplinski, and J. R. Mielenz. 2006. Measuring the efficiency of biomass energy. *Science*. 312:1744–1745.
4. Palmer, M. W., and M. Downing. 2006. Harvesting our meadows for biofuel? *Science*. 312:1745–1746.
5. Cleveland, C. J., C. A. S. Hall, R. A. Herendeen, N. Hagens, R. Costanza, K. Mulder, L. Lynd, N. Greene, B. Dale, M. Laser, D. Lashof, M. Wang, C. Wyman, R. K. Kaufman, T. W. Patzek, A. E. Farrell, R. J. Plevin, B. T. Turner, A. D. Jones, M. O'Hare, and D. M. Kammen. 2006. Energy returns on ethanol production. *Science*. 312: 1746–1748.
6. Zhou, T., Y. Mo, Z. Zhou, and K. Tsai. 2005. Density functional study on dihydrogen activation at the H cluster in Fe-only hydrogenases. *Inorg. Chem.* 44:4941–4946.
7. Brand, J. J., J. N. Wright, and S. Lien. 1989. Hydrogen production by eukaryotic algae. *Biotechnol. Bioeng.* 33:1482–1488.
8. Boichenko, V. A., E. Greenbaum, and M. Seibert. 2004. Hydrogen production by photosynthetic microorganisms. *In* Photoconversion of Solar Energy: Molecular to Global Photosynthesis. M. D. Archer and J. Barber, editors. Imperial College Press, London, UK.
9. Florin, L., A. Tsokoglou, and T. Happe. 2001. A novel type of iron hydrogenase in the green alga *Scenedesmus obliquus* is linked to the photosynthetic electron transport chain. *J. Biol. Chem.* 276:6125–6132.
10. Winkler, M., C. Mauerer, A. Hemschemeier, and T. Happe. 2004. The isolation of green algal strains with outstanding H_2-productivity. *In* Biohydrogen III. J. Miyake, Y. Igarashi, and M. Roegner, editors. Elsevier Science, Oxford, UK.
11. Winkler, M., A. Hemschemeier, C. Gotor, A. Melis, and T. Happe. 2002. [Fe]-Hydrogenases in green algae: photo-fermentation and hydrogen evolution under sulfur deprivation. *Int. J. Hydrogen Energ.* 27:1431–1439.
12. Melis, A., L. Zhang, M. Forestier, M. L. Ghirardi, and M. Seibert. 2000. Sustained photobiological hydrogen gas production upon reversible inactivation of oxygen evolution in the green alga *Chlamydomonas reinhardtii*. *Plant Physiol.* 122:127–135.
13. Tsygankov, A., S. Kosourov, M. Seibert, and M. L. Ghirardi. 2002. Hydrogen photoproduction under continuous illumination by sulfur-deprived, synchronous *Chlamydomonas reinhardtii* cultures. *Int. J. Hydrogen Energ.* 27:1239–1244.
14. Happe, T., and A. Kaminski. 2002. Differential regulation of the Fe-hydrogenase during anaerobic adaptation in the green alga *Chlamydomonas reinhardtii*. *Eur. J. Biochem.* 269:1022–1032.
15. Kosourov, S., M. Seibert, and M. L. Ghirardi. 2003. Effects of extracellular pH on the metabolic pathways in sulfur-deprived, H_2-producing *Chlamydomonas reinhardtii* cultures. *Plant Cell Physiol.* 44:146–155.
16. Forestier, M., P. King, L. Zhang, M. Posewitz, S. Schwarzer, T. Happe, M. L. Ghirardi, and M. Seibert. 2003. Expression of two [Fe]-hydrogenases in *Chlamydomonas reinhardtii* under anaerobic conditions. *Eur. J. Biochem.* 270:2750–2758.
17. Ghirardi, M. L. 2006. Hydrogen production by photosynthetic green algae. *Indian J. Biochem. Biophys.* 43:201–210.
18. Mus, F., L. Cournac, V. Cardettini, A. Caruana, and G. Peltier. 2005. Inhibitor studies on non-photochemical plastoquinone reduction and H_2 photoproduction in *Chlamydomonas reinhardtii*. *Biochim. Biophys. Acta Bioenerg.* 1708:322–332.
19. Posewitz, M. C., P. W. King, S. L. Smolinski, R. D. Smith II, A. R. Ginley, M. L. Ghirardi, and M. Seibert. 2005. Identification of genes required for hydrogenase activity in *Chlamydomonas reinhardtii*. *Biochem. Soc. Trans.* 33:102–104.
20. King, P. W., M. C. Posewitz, M. L. Ghirardi, and M. Seibert. 2006. Functional studies of [FeFe] hydrogenase maturation in an *Escherichia coli* biosynthetic system. *J. Bacteriol.* 188:2163–2172.
21. Posewitz, M. C., P. W. King, S. L. Smolinski, L. Zhang, M. Seibert, and M. L. Ghirardi. 2004. Discovery of two novel radical S-adenosylmethionine proteins required for the assembly of an active [Fe] hydrogenase. *J. Biol. Chem.* 279:25711–25720.
22. Appel, J., and R. Schulz. 1998. Hydrogen metabolism in organisms with oxygenic photosynthesis: hydrogenases as important regulatory devices for a proper redox poising? *J. Photochem. Photobiol. B Biol.* 47:1–11.

23. Erbes, D. L., D. King, and M. Gibbs. 1979. Inactivation of hydrogenase in cell-free extracts and whole cells of *Chlamydomonas reinhardtii* by oxygen. *Plant Physiol.* 63:1138–1142.

24. Ghirardi, M. L., R. K. Togaski, and M. Seibert. 1997. Oxygen sensitivity of algal H_2-production. *Appl. Biochem. Biotechnol.* 63: 141–151.

25. Tsygankov, A. A., S. N. Kosourov, I. V. Tolstygina, M. L. Ghirardi, and M. Seibert. 2006. Hydrogen production by sulfur-deprived *Chlamydomonas reinhardtii* under photoautotrophic conditions. *Int. J. Hydrogen Energ.* 31:1574–1584.

26. Flynn, T., M. L. Ghirardi, and M. Seibert. 2002. Accumulation of O_2-tolerant phenotypes in H_2-producing strains of *Chlamydomonas reinhardtii* by sequential applications of chemical mutagenesis and selection. *Int. J. Hydrogen Energ.* 27:1421–1430.

27. Cohen, J., K. Kim, P. King, M. Seibert, and K. Schulten. 2005. Finding gas diffusion pathways in proteins: application to O_2 and H_2 transport in CpI [FeFe]-hydrogenase and the role of packing defects. *Structure.* 13:1–9.

28. Cohen, J., K. Kim, M. Posewitz, M. L. Ghirardi, K. Schulten, M. Seibert, and P. King. 2005. Molecular dynamics and experimental investigation of H_2 and O_2 diffusion in [Fe]-hydrogenase. *Biochem. Soc. Trans.* 33:80–82.

29. Melis, A., and T. Happe. 2001. Hydrogen production. Green algae as a source of energy. *Plant Physiol.* 127:740–748.

30. Knaff, D. B. 1996. Ferredoxin and ferredoxin-dependent enzymes. *In* Oxygenic Photosynthesis: The Light Reactions. D. R. Ort and C. F. Yocum, editors. Kluwer Academic Publishers, Dordrecht, The Netherlands.

31. Decottignies, P., V. Flesch, C. Gérard-Hirne, and P. Le Maréchal. 2003. Role of positively charged residues in *Chlamydomonas reinhardtii* ferredoxin-NADP$^+$-reductase. *Plant Phys. Biochem.* 41:637–642.

32. Kurisu, G., D. Nishiyama, M. Kusunoki, S. Fujikawa, M. Katoh, G. T. Hanke, T. Hase, and K. Teshima. 2005. A structural basis of *Equisetum arvense* ferredoxin isoform II producing an alternative electron transfer with ferredoxin-NADP$^+$ reductase. *J. Biol. Chem.* 280:2275–2281.

33. Jelesarov, I., and H. R. Bosshard. 1994. Thermodynamics of ferredoxin binding to ferredoxin:NADP$^+$ reductase and the role of water at the complex interface. *Biochemistry.* 33:13321–13328.

34. Batie, C. J., and H. Kamin. 1984. Ferredoxin:NADP$^+$ oxidoreductase: equilibria in binary and ternary complexes with NADP$^+$ and ferredoxin. *J. Biol. Chem.* 259:8832–8839.

35. Batie, C. J., and H. Kamin. 1981. The relation of pH and oxidation-reduction potential to the association state of the ferredoxin·ferredoxin: NADP$^+$ reductase complex. *J. Biol. Chem.* 256:7756–7763.

36. De Pascalis, A. R., I. Jelesarov, F. Achkermann, W. H. Koppenol, M. Hirasawa, D. B. Knaff, and H. R. Bosshard. 1993. Binding of ferredoxin to ferredoxin:NADP$^+$ oxidoreductase: the role of carboxyl groups, electrostatic surface potential, and molecular dipole moment. *Protein Sci.* 2:1126–1135.

37. Karplus, P. A., and C. M. Bruns. 1994. Structure-function relations for ferredoxin reductase. *J. Bioenerg. Biomembr.* 26:89–99.

38. Kurisu, G., M. Kusunoki, E. Katoh, T. Yamazaki, K. Teshima, Y. Onda, Y. Kimata-Ariga, and T. Hase. 2001. Structure of the electron transfer complex between ferredoxin and ferredoxin-NADP$^+$ reductase. *Nat. Struct. Biol.* 8:117–121.

39. Hirasawa, M., M. Droux, K. A. Gray, J. M. Boyer, D. J. Davis, B. B. Buchanan, and D. B. Knaff. 1988. Ferredoxin-thioredoxin reductase: properties of its complex with ferredoxin. *Biochim. Biophys. Acta Bioenerg.* 935:1–8.

40. Swamy, U., M. Wang, J. N. Tripathy, S.-K. Kim, M. Hirasawa, D. B. Knaff, and J. P. Allen. 2005. Structure of spinach nitrite reductase: implications for multi-electron reactions by the iron-sulfur:siroheme cofactor. *Biochemistry.* 44:16054–16063.

41. Schnell, R., T. Sandalova, U. Hellman, Y. Lindqvist, and G. Schneider. 2005. Siroheme- and [Fe_4S_4]-dependent NirA from *Mycobacterium tuberculosis* is a sulfite reductase with a covalent Cys-Tyr bond in the active site. *J. Biol. Chem.* 280:27319–27328.

42. Saitoh, T., T. Ikegami, M. Nakayama, K. Teshima, H. Akutsu, and T. Hase. 2006. NMR study of the electron transfer complex of plant ferredoxin and sulfite reductase. *J. Biol. Chem.* 281:10482–10488.

43. Droux, M., J.-P. Jacquot, M. Miginac-Maslow, P. Gadal, J. C. Huet, N. A. Crawford, B. C. Yee, and B. B. Buchanan. 1987. Ferredoxin-thioredoxin reductase, an iron-sulfur enzyme linking light to enzyme regulation in oxygenic photosynthesis: purification and properties of the enzyme from C_3, C_4, and cyanobacterial species. *Arch. Biochem. Biophys.* 252:426–439.

44. Happe, T., and J. D. Naber. 1993. Isolation, characterization and N-terminal amino acid sequence of hydrogenase from the green alga *Chlamydomonas reinhardtii. Eur. J. Biochem.* 214:475–481.

45. Roessler, P. G., and S. Lien. 1984. Purification of hydrogenase from *Chlamydomonas reinhardtii. Plant Physiol.* 75:705–709.

46. Papoian, G. A., J. Ulander, and P. G. Wolynes. 2003. Role of water-mediated interactions in protein-protein recognition landscapes. *J. Am. Chem. Soc.* 125:9170–9178.

47. Guex, N., and M. C. Peitsch. 1997. SWISS-MODEL and the Swiss-PDB viewer: an environment for comparative protein modeling. *Electrophoresis.* 18:2714–2723.

48. Humphrey, W., A. Dalke, and K. Schulten. 1996. VMD—visual molecular dynamics. *J. Mol. Graph.* 14:33–38.

49. Schmitter, J.-M., J.-P. Jacquot, F. de Lamotte-Guéry, C. Beauvallet, S. Dutka, P. Gadal, and P. Decottignies. 1988. Purification, properties and complete amino acid sequence of the ferredoxin from a green algal, *Chlamydomonas reinhardtii. Eur. J. Biochem.* 172:405–412.

50. Stein, M., J.-P. Jacquot, and M. Miginiac-Maslow. 1993. A cDNA clone encoding *Chlamydomonas reinhardtii* preferredoxin. *Plant Physiol.* 102:1349–1350.

51. Peitsch, M. C. 1995. Protein modeling by e-mail. *Biotechnology.* 13: 658–660.

52. Schwede, T., J. Kopp, N. Guex, and M. C. Peitsch. 2003. SWISS-MODEL: an automated protein homology-modeling server. *Nucleic Acids Res.* 31:3381–3385.

53. Guex, N., and M. C. Peitsch. 2003. SWISS-MODEL and the Swiss-PDB viewer: an environment for comparative protein modeling. *Electrophoresis.* 18:2714–2723.

54. Gabb, H. A., R. M. Jackson, and M. J. E. Sternberg. 1997. Modeling protein docking using shape complementarity, electrostatics and biochemical information. *J. Mol. Biol.* 272:106–120.

55. Moont, G., H. A. Gabb, and M. J. E. Sternberg. 1999. Use of pair potentials across protein interfaces in screening predicted docked complexes. *Protein Struct. Funct. Genet.* 35:364–373.

56. Koehl, P., and M. Delarue. 1994. Application of a self-consistent mean field theory to predict protein side-chains conformation and estimate their conformational entropy. *J. Mol. Biol.* 239:249–275.

57. Katchalski-Katzir, E., I. Shariv, M. Eisenstein, A. A. Friesem, C. Aflalo, and I. A. Vakser. 1992. Molecular surface recognition: determination of geometric fit between proteins and their ligands by correlation techniques. *Proc. Natl. Acad. Sci. USA.* 89:2195–2199.

58. Jones, S., and J. M. Thornton. 1996. Principles of protein-protein interactions. *Proc. Natl. Acad. Sci. USA.* 93:13–20.

59. Ray, N., X. Cavin, J.-C. Paul, and B. Maigret. 2005. Intersurf: dynamic interface between proteins. *J. Mol. Graph.* 23:347–354.

60. Frishman, D., and P. Argos. 1995. Knowledge-based protein secondary structure assignment. *Protein Struct. Funct. Genet.* 23:566–579.

61. Noskov, S. Y., and C. Lim. 2001. Free energy decomposition of protein-protein interactions. *Biophys. J.* 81:737–750.

62. McQuarrie, D. A. 1973. Statistical Mechanics. HarperCollins, New York.

63. Humphrey, W., A. Dalke, and K. Schulten. 1996. VMD—visual molecular dynamics. *J. Mol. Graph.* 14:33–38.

64. Laxmikant, K., R. Skeel, M. Bhandarkar, R. Brunner, A. Gursoy, N. Krawetz, J. Phillips, A. Shinozaki, K. Varadarajan, and K. Schulten. 1999. NAMD2: greater scalability for parallel molecular dynamics. *J. Comput. Phys.* 151:283–312.

65. Xiang, T.-x., F. Liu, and D. M. Grant. 1991. Generalized Langevin equations for molecular dynamics in solution. *J. Chem. Phys.* 94:4463–4471.

66. Adcock, S. A., and J. A. McCammon. 2006. Molecular dynamics: survey of methods for simulating the activity of proteins. *Chem. Rev.* 106:1589–1615.

67. Darden, T., D. York, and L. Pedersen. 1993. Particle mesh Ewald: an $N \cdot \log(N)$ method for Ewald sums in large systems. *J. Chem. Phys.* 98:10089–10092.

68. Essmann, U., L. Perera, M. L. Berkowitz, T. Darden, H. Lee, and L. G. Pedersen. 1995. A smooth particle mesh Ewald method. *J. Chem. Phys.* 103:8577–8593.

69. Tuckerman, M., B. J. Berne, and G. J. Martyna. 1992. Reversible multiple time scale molecular dynamics. *J. Chem. Phys.* 97:1990–2001.

70. Watanabe, M., and M. Karplus. 1995. Simulations of macromolecules by multiple time-step methods. *J. Phys. Chem.* 99:5680–5697.

71. Andersen, H. C. 1983. RATTLE: a velocity version of the SHAKE algorithm for molecular dynamics calculations. *J. Comput. Phys.* 52: 24–34.

72. Miyamoto, S., and P. A. Kollman. 1992. SETTLE: an analytical version of the SHAKE and RATTLE algorithm for rigid water models. *J. Comput. Chem.* 13:952–962.

73. Still, W. C., A. Tempczyk, R. C. Hawley, and T. Hendrickson. 1990. Semianalytical treatment of solvation for molecular mechanics and dynamics. *J. Am. Chem. Soc.* 112:6127–6129.

74. Lee, M. S., M. Feig, F. R. Salsbury, Jr., and C. L. Brooks III. 2003. New analytic approximation to the standard molecular volume definition and its application to generalized Born calculations. *J. Comput. Chem.* 24:1348–1356.

75. Nilsson, L., and M. Karplus. 1986. Empirical energy functions for energy minimization and dynamics of nucleic acids. *J. Comput. Chem.* 7:591–616.

76. Dominy, B. N., and C. L. Brooks III. 1999. Development of a generalized Born model parameterization for proteins and nucleic acids. *J. Phys. Chem. B.* 103:3765–3773.

77. Baker, N. A., D. Sept, S. Joseph, M. J. Holst, and J. A. McCammon. 2001. Electrostatics of nanosystems: application to microtubules and the ribosome. *Proc. Natl. Acad. Sci. USA.* 98:10037–10041.

78. Dolinsky, T. J., J. E. Nielsen, J. A. McCammon, and N. A. Baker. 2004. PDB2PQR: an automated pipeline for the setup, execution, and analysis of Poisson-Boltzmann electrostatics calculations. *Nucleic Acids Res.* 32:W665–W667.

79. Lee, B., and F. M. Richards. 1971. The interpretation of protein structures: estimation of static accessibility. *J. Mol. Biol.* 55:379–400.

80. Karplus, M., and J. N. Kushick. 1981. Method for estimating the configurational entropy of macromolecules. *Macromolecules.* 14:325–332.

81. Brooks, B. R., D. Janežic, and M. Karplus. 1995. Harmonic analysis of large systems. I. Methodology. *J. Comput. Chem.* 16:1522–1542.

82. Janežic, D., and B. R. Brooks. 1995. Harmonic analysis of large systems. II. Comparison of different protein models. *J. Comput. Chem.* 16:1543–1553.

83. Zhang, Y., and J. A. McCammon. 2003. Studying the affinity and kinetics of molecular association with molecular-dynamics simulation. *J. Chem. Phys.* 118:1821–1827.

84. Lo Conte, L., C. Chothia, and J. Janin. 1999. The atomic structure of protein-protein recognition sites. *J. Mol. Biol.* 285:2177–2198.

85. Vieira, B. J., K. K. Colvert, and D. J. Davis. 1986. Chemical modification and cross-linking as probes of regions on ferredoxin involved in its interaction with ferredoxin: NADP reductase. *Biochim. Biophys. Acta Bioenerg.* 851:109–122.

86. Schmitz, S., and H. Böhme. 1995. Amino acid residues involved in functional interaction of vegetative cell ferredoxin from the cyanobacterium *Anabaena* sp. PCC 7120 with ferredoxin:NADP reductase, nitrite reductase and nitrate reductase. *Biochim. Biophys. Acta Bioenerg.* 1231:335–341.

87. Akashi, T., T. Matsamura, T. Ideguchi, K.-i. Iwakiri, T. Kawakatsu, I. Taniguchi, and T. Hase. 1999. Comparison of the electrostatic binding sites on the surface of ferredoxin for two ferredoxin-dependent enzymes, ferredoxin-NADP$^+$ reductase and sulfite reductase. *J. Biol. Chem.* 274:29399–29405.

88. Privalle, L. S., C. T. Privalle, N. J. Leonardy, and H. Kamin. 1985. Interactions between Spinach ferredoxin-nitrite reductase and its substrates—evidence for the specificity of ferredoxin. *J. Biol. Chem.* 260:14344–14350.

89. Palma, P. N., B. Lagoutte, L. Krippahl, J. J. G. Moura, and F. Guerlesquin. 2005. *Synechocystis* ferredoxin/ferredoxin-NADP$^+$-reductase/NADP$^+$ complex: structural model obtained by NMR-restrained docking. *FEBS Lett.* 579:4585–4590.

90. García-Sánchez, M. I., C. Gotor, J.-P. Jacquot, M. Stein, A. Suzuki, and J. M. Vega. 1997. Critical residues of *Chlamydomonas reinhardtii* ferredoxin for interaction with nitrite reductase and glutamate synthase revealed by site-directed mutagenesis. *Eur. J. Biochem.* 250:364–368.

91. Gray, H. B., and J. R. Winkler. 2005. Long-range electron transfer. *Proc. Natl. Acad. Sci. USA.* 102:3534–3539.

92. Hush, N. S. 1985. Distance dependence of electron-transfer rates. *Coord. Chem. Rev.* 64:135–157.

93. Marcus, R. A., and N. Sutin. 1985. Electron transfers in chemistry and biology. *Biochim. Biophys. Acta.* 811:265–322.

94. Fan, H.-J., and M. B. Hall. 2001. A capable bridging ligand for Fe-only hydrogenase: density functional calculations of a low-energy route for heterolytic cleavage and formation of dihydrogen. *J. Am. Chem. Soc.* 123:3828–3829.

95. Nicolet, Y., A. L. de Lacey, X. Vernède, V. M. Fernandez, E. C. Hatchikian, and J. C. Fontecilla-Camps. 2001. Crystallographic and FTIR spectroscopic evidence of changes in Fe coordination upon reduction of the active site of the Fe-only hydrogenase from *Desulfovibrio desulfuricans. J. Am. Chem. Soc.* 123:1596–1601.

96. Nicolet, Y., C. Piras, P. Legrand, C. E. Hatchikian, and J. C. Fontecilla-Camps. 1999. *Desulfovibrio desulfuricans* iron hydrogenase: the structure shows unusual coordination to an active site Fe binuclear center. *Structure.* 7:13–23.

97. Zampella, G., C. Greco, P. Fantucci, and L. De Gioia. 2006. Proton reduction and dihydrogen oxidation on models of the $[2Fe]_H$ cluster of [Fe] hydrogenases. A density functional theory investigation. *Inorg. Chem.* 45:4109–4118.

98. Greco, C., G. Zampella, L. Bertini, M. Bruschi, P. Fantucci, and L. De Gioia. 2007. Insights into the mechanism of electrocatalytic hydrogen evolution mediated by $Fe_2(S_2C_3H_6)(CO)_6$: the simplest functional model of the Fe-hydrogenase active site. *Inorg. Chem.* 46:108–116.